DALHOUSIE UNIVERSITY

An experimental study of the effect of water on chromite solubility in komatiites

Kate Woods

SUBMITTED IN PARTIAL FULFILLMENT OF THE REQUIREMENTS FOR
THE DEGREE OF BACHELOR OF SCIENCE, HONOURS
DEPARTMENT OF EARTH SCIENCES
DALHOUSIE UNIVERSITY, HALIFAX, NOVA SCOTIA

April 2018

Table of Contents

List of Tables

List of Figures

Abstract

Chromite ($FeCr_2O_4$) is an oxide mineral and common accessory phase in ultramafic rocks. More unusually, chromite occurs in concentrated strata or lenses within layered mafic intrusions. The komatiite-hosted Blackbird Chromite deposit, located near McFaulds Lake in the James Bay Lowlands, Ontario, is one of five known chromite deposits within the Ring of Fire intrusive complex, and is the subject of this study. Chromite is the only chromium ore, and such deposits have great economic importance. Despite this, the conditions of formation of large chromite deposits are poorly constrained. The purpose of this investigation is to characterize the effect of magmatic water on the mineral phase relationships in komatiitic magmas. Anhydrous studies of komatiites have shown that olivine is the earliest-crystallizing phase in these magmas. It is known from studies of more felsic melt compositions that, while magmatic water inhibits crystallization of most silicate phases, it has a relatively lesser impact on oxide stability. Orthopyroxene, an important constituent in komatiites, readily accepts chromium into its structure, such that early-crystallizing pyroxene can prevent chromite from precipitating. Water is hypothesized to promote chromite crystallization by suppressing the growth of silicate phases that might otherwise compete for chromium in the melt, thereby extending the interval over which chromite may then accumulate, possibly as the only crystalline phase. Calculated phase equilibria suggest that, for magmatic water content greater than 3.5 wt%, the olivine liquidus may be sufficiently depressed to allow chromite to form as the sole liquidus phase. Experiments using synthetic komatiite with up to 4 wt% added H_2O and varied Cr contents have been equilibrated at temperatures ranging from 1350-1600°C. To accommodate water, experimental materials were sealed in graphite-lined platinum capsules and pressurized to 1 GPa in a piston-cylinder apparatus. Results from this study show that magmatic water increases the solubility of chromium in a komatiitic magma, which may have implications as a mechanism for chromium transfer.

Keywords: chromite, komatiite, experimental petrology, economic geology, ore petrology

List of Mineral Abbreviations

Chromite	chr
Clinopyroxene	cpx
Glass	gl
Liquid (melt)	liq
Olivine	ol
Orthopyroxene	opx
Spinel	sp

Acknowledgements

I would like to acknowledge the Targeted Geosciences Initiative, the Shell Experiential Learning Fund, and the Society of Economic Geologists Canada Foundation for their generous financial support toward this project.

Thank you to James Brenan for his patience and guidance over the course of this year.

Thank you to my labmates, Erin, Bryan, and Xueni, for supporting me.

Chapter 1: Introduction

The purpose of this study is to determine the effect of water on chromite solubility in komatiitic magma. Although komatiites are associated with economic deposits called massive chromitites, such as those observed in the Ring of Fire Intrusive Suite (ROFIS) in Ontario, the mechanisms by which these deposits form are poorly constrained and much debated. Several hypotheses have been posited, however, the original work in this study is focussed on the effect of water.

1.1 Komatiites

Komatiites are the oldest primary mantle-derived melts, now rocks, on Earth. With few exceptions, komatiites are Archean in age. They are a product of high degrees (up to 30-40%; Grove and Parman 2004) of mantle melting possible only in a substantially younger, hotter Earth (Parman *et al.* 1997). Komatiites were originally described as peridotitic lavas and named for the locale of their discovery (Viljoen and Viljoen 1969). Komatiitic lavas exhibit a distinctive spinifex texture and are easily distinguished from other types of ultramafic rocks by their relict glassy matric, interspersed with skeletal olivine and sometimes clinopyroxene megacrysts (Viljoen and Viljoen 1969; Arndt *et al.* 1977). Komatiites may also occur as intrusive bodies.

Current literature defines komatiites as ultramafic (>18 wt% MgO) magmas, which are subdivided into alumina-depleted or 'Barberton-type' komatiites, and alumina-undepleted 'Munro-type' komatiites (Arndt 2003; Arndt *et al.* 1977; Nesbitt *et al.* 1979). The alumina content of a komatiite is likely related to the depth of the melting that produced it, and whether the melting occurred in equilibrium with Al-rich garnet (Nesbitt *et al.* 1979). This interpretation is supported by rare Earth element (REE) signatures indicative of garnet in the residuum of the Barberton, but not Munro komatiites (Nesbitt *et al.* 1979). Munro-type komatiites are the product of shallower, and possibly hydrous (Arndt 2003) mantle melting than Barberton-types.

The textural and chemical variability observed in komatiites may reflect the different magmatic and tectonic environments that produced them. The majority of komatiites have been

observed as having extruded as lavas (Arndt *et al.* 1979). Some are laterally extensive sheeted flows, while others are very thick, sometimes ponded-type flows or lava lakes (Arndt 1977; Barnes 1998). Komatiitic intrusions are commonly observed as repetitive sill-like bodies (Mungall *et al.* 2016). One commonality in natural komatiites is that, invariably and regardless of their form, these ancient rocks have been metamorphosed, metasomatized, or otherwise chemically altered since the time of their emplacement.

Experimental investigations of komatiite phase equilibria have been conducted mostly with anhydrous compositions at atmospheric pressure (Kinzler and Grove 1985; Thy 1995). Under these conditions, olivine is always the first phase on the liquidus in a komatiitic magma, followed by chromite, then a pyroxene (Kinzler and Grove 1985; Thy 1995). This crystallization path is also observed in studies of simplified komatiitic systems (Faure *et al.* 2006). Liquidus temperatures have been estimated to be as great as 1650°C for the most magnesian komatiites (Green *et al.* 1975). Water saturation has been estimated to depress the liquidus of a given komatiite by as much as 200°C (Parman *et al.* 1997). The spinifex textures observed in natural komatiites have been reproduced under laboratory conditions and their formation appears to be facilitated by the presence of water (Parman *et al.* 1997) and the imposition of a thermal gradient (Bouquain *et al.* 2014; Faure *et al.* 2006).

1.2 Chromite

Chromium is an essential component in stainless steel, and has a wide range of applications in metallurgy, pigments, and even as a wood preservative. Chromite ($FeCr_2O_4$) is the only chromium ore. Omnipresent as an accessory phase in mafic rocks, chromite is more rarely observed as cumulate sheets, lenses, or pods, called massive chromitites. Historically, chromitites have been divided into two broad categories (Stowe 1994). Stratiform deposits are those which form in the lower sequences of a layered mafic intrusion (Stowe 1994). Podiform or ‘alpine-type’ chromitites are associated with metasomatically altered ultramafics in ophiolite sequences (Stowe 1994). A third designation, the conduit-hosted chromitite, is entering the lexicon and represents a compelling area of current research (Christyakova *et al.* 2015; Yudovskaya *et al.* 2015).

The formation mechanisms of massive chromitites are poorly understood. Several hypotheses exist to explain their occurrence, including magma mixing (Irvine 1975; Irvine 1977); crustal assimilation (Mungall *et al.* 2010); mechanical separation of phases (Christyakova *et al.* 2015); transient changes in pressure (Lipin 1993); and the effects of water on phase relations in the magma (Nicholson and Mathez 1990). Conduit-hosted deposits are especially likely to have formed in dynamic environments, with localized variations in melt composition and oxidation state (oxygen fugacity, fO_2) imposed on the crystallizing melt by interaction with and assimilation of the host rock. In order to better understand how a conduit-hosted chromitite forms, it is necessary to isolate parameters for experimental investigation. In this study, the explanatory variable of interest is the water content of the melt.

The appearance of chromite marks the point of chromium saturation in a given melt (Barnes 1986; Kinzler and Grove 1985; Murck and Campbell 1986; Roeder and Reynolds 1991). The relationship between melt composition and chromium solubility is illustrated in Figure 1 (Barnes 1998). Chromite is a normal spinel of the form $A(B_2)O_4$, with trivalent cations in octahedral sites (B) and divalent cations in tetrahedral sites (A) (Murck and Campbell 1986; Roeder and Reynolds 1991). Chromium has a strong octahedral site preference, which results in only Cr^{3+}, and no Cr^{2+}, entering the spinel structure (Murck and Campbell 1986; Roeder and Reynolds 1991). Chromium solubility is strongly dependent on the oxygen fugacity of the melt, which controls the ratio of Cr^{2+}/Cr^{3+} and therefore the availability of chromium compatible in the spinel structure (Barnes 1986; Murck and Campbell 1986; Roeder and Reynolds 1991).

Previous experimental studies on phase relations in komatiites have shown that, under anhydrous conditions, olivine is the first phase to crystallize (Kinzler and Grove 1985; Parman et al. 1997). It is typically followed by chromite, then pyroxene (Kinzler and Grove 1985). The abundance of chromite is limited by the low solubility of chromium, which reaches a maximum of only a few thousand ppm under normal magmatic conditions (Figure 1, Barnes 1998). Because chromium is compatible in the pyroxene structure, the onset of pyroxene crystallization effectively prevents the further accumulation of chromite in the magma (Irvine 1975). Given these barriers to chromitite formation under normal circumstances, it is necessary to identify the conditions under which chromite precipitation is favoured while silicate precipitation is

suppressed. Indeed, chromite is an ubiquitous accessory mineral in komatiites, but is also – if only rarely – observed as monomineralic cumulates.

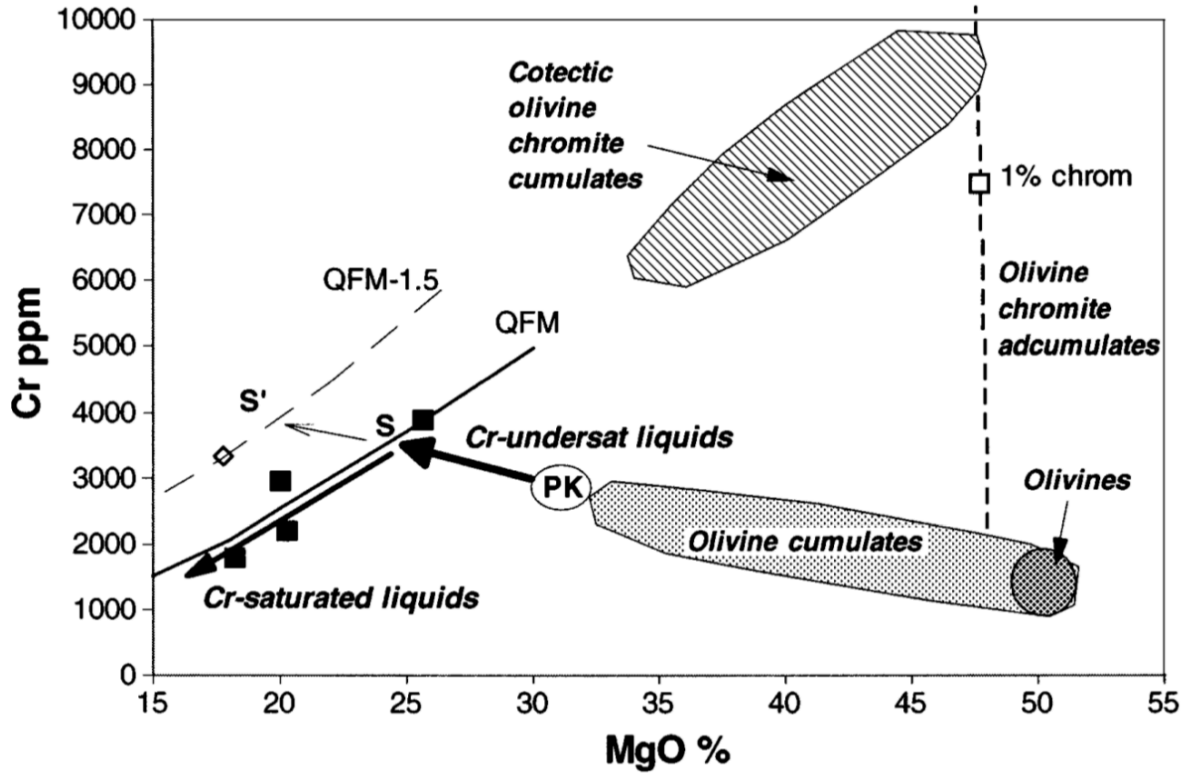

Figure 1. Diagram illustrating the variation in Cr as a function of MgO for natural komatiites and related cumulate rocks, along with the estimated chromite saturation surface at Quartz-Fayalite-Magnetite (FMQ) and FMQ-1.5 (from Barnes 1998).

1.3 Role of water in oxide crystallization in magma

It is difficult to draw any direct comparison between previous studies and this one, because the experimental conditions have been different. Although existing data are limited, all available evidence shows that the typical crystallization path for a komatiite produces olivine first and in greatest abundance, followed by accessory chromite. One study that explored the effects of water on phase relations in a komatiite, while focussed on the pyroxene and not liquidus phase equilibria, showed that the addition of 6 wt% H_2O to the melt composition did not prevent chromite crystallization, but did significantly lower pyroxene-in temperatures (Parman *et*

al. 1997). This is one mechanism by which the temperature interval of chromite precipitation may be extended.

Magmatic water has also been invoked as a mechanism by which chromite could precipitate from a melt as the sole liquidus phase in a melt that, under anhydrous conditions, would otherwise saturate first in a silicate phase (Nicholson and Mathez 1990). Studies of basaltic systems have shown that water exerts a greater effect on the crystallization temperatures of silicate phases than on non-silicates like spinel group minerals (Sisson and Grove 1993). Sisson and Grove found that the addition of water to basalts could induce magnetite, another spinel mineral, to appear as the liquidus phase, as illustrated in Figure 2 (1993).

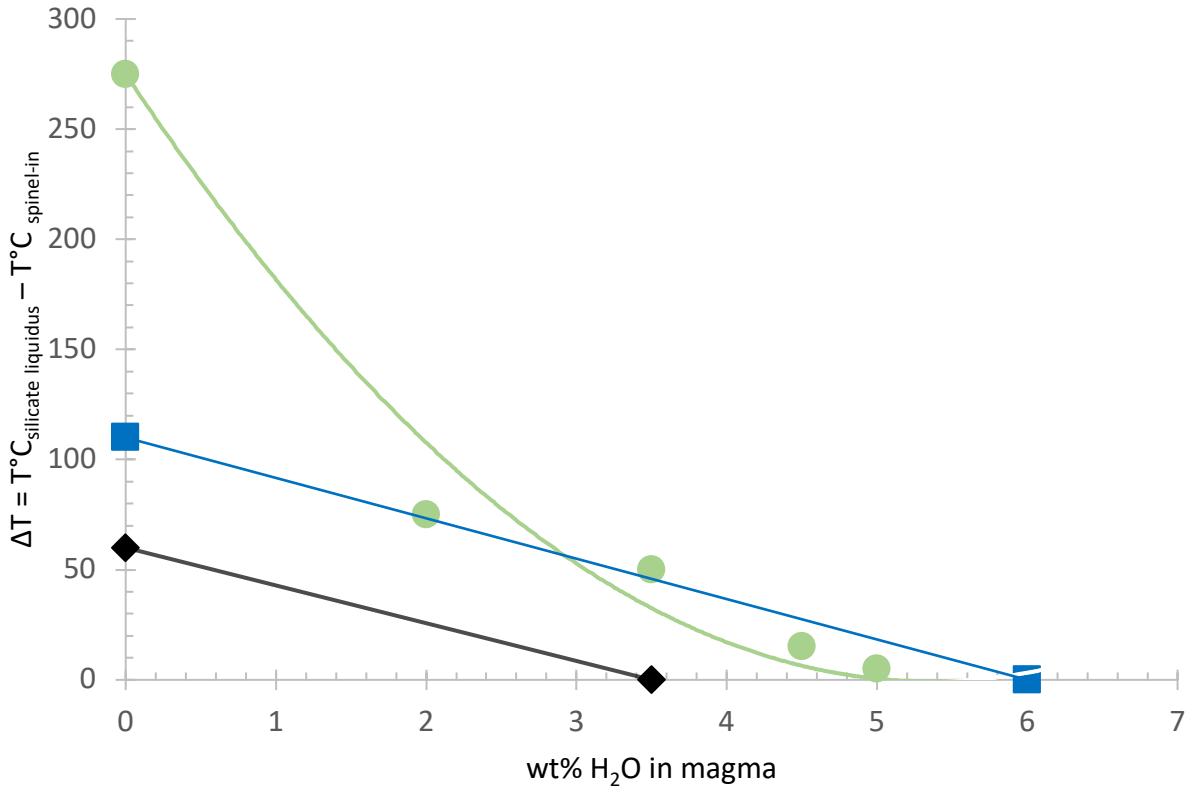

Figure 2. Diagram illustrating the depression of the silicate liquidus relative to the oxide-in temperature in basaltic magmas (after Sisson and Grove 1991). Where $\Delta T = 0$, the silicate-spinel crystallization order is reversed, such that the spinel phase (magnetite) is the first to crystallize. This occurs with the addition of between 3.5 and 6 wt% H_2O to the experimental melt.

The presence, source, and importance of water in komatiites is an issue of contention (Arndt 1998). Unambiguous evidence for water in komatiites has been observed as vesicles, hydrous melt inclusions, and primary magmatic amphiboles (Arndt 1998; Fiorentini *et al.* 2012; Shimizu *et al.* 2001; Stone *et al.* 2002). The heavy ∂D isotopic signatures of some hydrous komatiites point to a mantle origin for at least some water (Arndt 1998; Fiorentini *et al.* 2012). This water may have been entrained at the mantle transition zone, as evidenced by B isotopic signatures measured in melt inclusions in Munro-type komatiites from Pyke Hill and Munro Township, Ontario (Sobolev et al. 2016). Even extrusive komatiites, if erupted in a sufficiently deep submarine setting, may have retained up to 0.5 wt% H_2O (Green *et al.* 1975). Magmatic water can destabilize garnet in a peridotitic melt and has been implicated as one of the factors contributing to the formation of Munro-type komatiites (Arndt 2003).

Water might also be entrained as the komatiite travelled through and thermally eroded its host rock. Komatiites erupted or were emplaced at exceptionally high temperatures, and many, including the Ring of Fire komatiite, show evidence of significant crustal contamination (Mungall *et al.* 2010). It is reasonable, then, to envision a komatiitic intrusion with some amount, or more likely, spatio-temporally variable amounts of water. In the context of this study, it is not critical to ascertain the source of water in the komatiite, be it primary or entrained. Hydrous melt inclusions in Ring of Fire chromite indicate that water was present in the melt at the time of spinel crystallization (Mungall *et al.* 2010).

Chapter 2: Modelling Methods

To guide the experiments, a simple phase diagram was first calculated in an effort to predict the conditions at which either olivine or chromite crystallizes first in the chosen komatiite composition. The models provide a means to identify experimental conditions of interest. The olivine- and chromite-in temperatures were calculated using MELTS (Ghiorso and Sack 1995) and SpinMelt-2 (Nikolaev *et al.* 2018a), respectively. Input variables (composition, pressure, and fO_2) were identical for both series of calculations, such that both liquidus curves could be projected onto the same T-H_2O plane. The pressure was fixed at 1 GPa and fO_2 varied with temperature, buffered by C-COH in the MELTS program and manually and iteratively matched to approximately the same fO_2 conditions (Ulmer and Luth 1991) in the SpinMelt-2 program. Water contents for both programs varied from 0 to 4 wt%. The melt composition was chosen based on previously modelled parent magma to the Ring of Fire komatiite (Azar 2010), with the Cr content adjusted to reflect the 'theoretical Cr-MgO compositions of komatiites' produced by Barnes (1998).

The MELTS software package was developed to model mass transfer in igneous systems (Ghiorso and Sack 1995). The software algorithm predicts the stable phase assemblage in a silicate magma of a given composition over user-specified pressure and temperature intervals (Ghiorso and Sack 1995). The algorithm uses singular value decompositions, a type of principal component analysis, to minimize the subset of independent variables, which are then incorporated into the non-linear optimization to predict the free energy state of the system (Ghiorso and Sack 1995). Olivine-in curves were calculated using rhyolite-MELTS v 1.2.0. This is the most recent version of MELTS that has been calibrated for magmatic systems containing dissolved H_2O ($\pm CO_2$) that are quartz-undersaturated, which was the most appropriate calibration for the magma composition of this study (Gualda *et al.* 2012; Ghiorso and Gualda 2015).

MELTS software can predict the silicate liquidus to within a reported accuracy of 10°C and programs in the MELTS family are useful for modelling silicate phase relationships (Ghiorso and Sack 1995). The MELTS family over-estimate the spinel liquidus temperature by an unacceptably large average of 300°C (Nikolaev *et al.* 2018a). For this reason, the chromite-in curves were constructed using SpinMelt-2 (Nikolaev *et al.* 2018a; Nikolaev *et al.* 2018b).

SpinMelt-2 is an iterative modelling software developed specifically to predict spinel phase equilibrium in magmatic systems (Nikolaev *et al.* 2018a; Nikolaev *et al.* 2018b). This program solves for stoichiometric relations (activities) of spinel components and their temperature-dependent reaction constants at user-specified temperature, pressure, fO_2, and melt composition (Nikolaev *et al.* 2018a) to estimate the equilibrium compositions of the spinel and remaining melt.

While the authors of SpinMelt-2 address some of the limitations of the MELTS program, its calibration was primarily based on intermediate-basaltic experimental data (Nikolaev *et al.* 2018a). Hydrous experimental systems were included only if they were water-saturated, and the komatiitic data included in the calibration data set were all anhydrous and run at atmospheric pressure (Nikolaev *et al.* 2018). The authors caution that hydrous melt compositions with less than 2.5 wt% H_2O are outside of the calibration data set. The calculation of spinel equilibria requires extrapolation to a hydrous komatiitic system at 1 GPa. Still, by combining the strengths of each modelling program, it was possible to produce a provisional phase diagram with which to guide experiments.

Chapter 3: Experimental Methods

Phase equilibrium experiments were performed with synthetic komatiite at 1 GPa and a range of temperatures using graphite-lined Pt capsules in a piston-cylinder apparatus to investigate (1) the effect of H_2O on oxide-silicate phase relations and (2) the effect of H_2O on chromium solubility.

3.1 Experimental starting materials

Natural komatiites are highly altered, usually serpentinized, and therefore unsuitable for use as experimental material. All experimental materials in this study were synthesized from high-purity reagents in the laboratory, allowing a high degree of control and ensuring a uniform composition with only the "chromite" and/or water contents varying between experiments. The melt composition was chosen based on a previously modelled parent magma to the komatiite-hosted Blackbird chromitite in the Ring of Fire, James Bay Lowlands, northern Ontario (Azar 2010; Mungall *et al.* 2010).

The Blackbird chromite deposit is hosted in a series of ca. 2.7 Ga mafic to ultramafic sills and conduits intruded into the metasedimentary and metavolcanic country rock of the Oxford-Stull domain in the Superior Province (Mungall *et al.* 2010). The Blackbird deposit is one of several such deposits in the ROFIS (Mungall *et al.* 2010). The parental melt was modelled based on chilled margin compositions to contain 23 wt% MgO, 45 wt% SiO_2, and 12 wt% FeO (Azar 2010; Mungall *et al.* 2010). This is the composition synthesized for use in this study (Table 1).

Starting materials (SM) were synthesized using high-purity powdered metallic oxides and carbonate salts. Reagents were weighed, mixed by grinding twice under ethanol with an agate mortar and pestle, and dried. Dried mixtures were calcined in a platinum crucible by heating in a box furnace in air at a ramp rate of 100°C per hour from 500°C to 1000°C, then held overnight. After calcining, materials were fused in air at 1500°C for 30 minutes then quenched in water to produce a homogeneous glass. The glass was extracted, ground, fused a second time, and the

final product ground to a fine powder. Composition was confirmed by electron microprobe analysis using a retained sample of the second fusion product.

For the experiments reported here, water was added as $Mg(OH)_2$. The stoichiometry of the $Mg(OH)_2$ reagent was determined by loss on ignition, assuming the reaction:

$$Mg(OH)_2 \Leftrightarrow Mg + H_2O \quad (1)$$

and was found to be 99.7% Mg(OH)2 and 0.3% MgO. Whereas adding $Mg(OH)_2$ to the anhydrous starting material would shift the MgO content of the komatiite, anhydrous starting material was prepared from a MgO-free komatiite synthesized as above. Aliquots containing 1, 2, and 4 wt% H_2O were prepared by adding the appropriate proportions of $Mg(OH)_2$ and MgO to the komatiite glass, then grinding under ethanol. This method produced homogeneous, hydrous starting materials of fixed H_2O contents and MgO content equal to that of the anhydrous starting material.

In the first series of experiments, water was added as a liquid using a micro-syringe. Graphite crucibles were weighed before and after adding the powdered glass, then again after adding H_2O, to give the wt% of H_2O added to the experiment. This method produced undesirable uncertainties in water contents of the experiments and was abandoned in favour of adding water as a solid phase.

In addition to the original komatiite (KO17) with ~2100 ppm Cr, three chromite-added compositions were prepared. These compositions were achieved by mixing, as above, powdered Fe_2O_3 and Cr_2O_3 in the stoichiometric proportions of chromite and adding each of 0.5, 1.0 and 2.0 wt% of this mixture to aliquots of the original starting materials. These chromite-doped compositions translate to initial melt Cr contents of ~2300, 4600, and 9200 ppm. The purpose of these Cr-rich compositions is to ensure chromite saturation would be reached at experimental conditions, as guided by previous studies on Cr solubility (Murck and Campbell 1986; Roeder and Reynolds 1991).

Table 1. Starting material compositions (EMPA)

SM	SiO_2	TiO_2	Al_2O_3	FeO	Cr_2O_3	MnO	MgO	CaO	Na_2O	K_2O	Tot
KO17	44.26	0.45	9.07	12.21	0.31	0.22	23.55	8.82	0.50	0.78	100.18
1σ	0.21	0.04	0.09	0.12	0.04	0.02	0.09	0.10	0.02	0.04	0.22
NoMg	57.48	11.57	0.57	15.84	0.42	0.30	0.01	11.09	0.64	1.00	98.91
1σ	0.54	0.09	0.05	0.41	0.03	0.03	0.01	0.14	0.02	0.04	0.26

3.2 Piston-cylinder apparatus and experimental assemblies

Experiments were done at 1 GPa and temperatures ranging from 1350-1450°C using graphite-lined Pt capsules in a piston-cylinder apparatus. Most experiments were run in a pressure vessel with a 19.05 mm bore, using crushable MgO, pyrex, and NaCl as the pressure media, with three samples in each. Experiments done at temperatures in excess of 1400°C were run singly in 12.70 mm assemblies, with crushable MgO and $BaCO_3$ sleeves as the pressure media. Temperature was monitored using a W-Re thermocouple, insulated by Al_2O_3 and placed as near to the hot-spot as possible within the sample assembly. Assemblies were heated internally using a cylindrical graphite furnace, with capsules centred along the axis to minimize thermal gradient effects. During experiments, pressure was found to drift and was adjusted periodically. Load applied to the piston included a 10% addition to the nominal value to account for friction between the piston and the sample assembly.

The graphite crucibles were machined from high-density graphite rods to 2.7 mm external diameter (the internal diameter of the Pt tubing), with 1.2 mm diameter bores. Graphite caps were machined similarly, to size; each graphite cap was fit to the crucibles by a 1.2 mm plug. Graphite components were cleaned ultrasonically in acetone, then dried before use. After machining, MgO was fired at 1000°C for 10-15 min to remove volatile contaminants.

The graphite crucibles were initially prepared with an 8 mm bore depth. This was necessary to accommodate the minimum amount of liquid water, about 0.05 μL, that could be accurately dispensed by a 0.5 μL syringe. Subsequent to the adoption of solid phase starting materials, the bore length was reduced to 5 mm, then 3.5 mm, to minimize the effects of the thermal gradient within the graphite furnace (Watson *et al.* 2002).

Pt capsules were cut from 3 mm tubing, cleaned by boiling in HCl, annealed, and sealed at one end by welding a 3-point crimp prior to loading. Each graphite crucible was filled, closed, and loaded top-down into the platinum capsule. Anhydrous experiments were crimped lightly then held at 106°C for a minimum of 96h before sealing and welded while hot, to prevent contamination by atmospheric water.

Except for experiments KW5-1, KW5-2, and KW5-3, all were run for 6 hours. This run time was sufficient to achieve equilibrium while short enough to prevent complications due to thermocouple oxidation at very high temperatures. Brass, instead of steel, base plugs were employed in both 19.05 mm and 12.70 mm assemblies to preserve thermocouple integrity. Experiments KW5-1, KW5-2, and KW5-3 were quenched after 1 hour due to thermocouple failure.

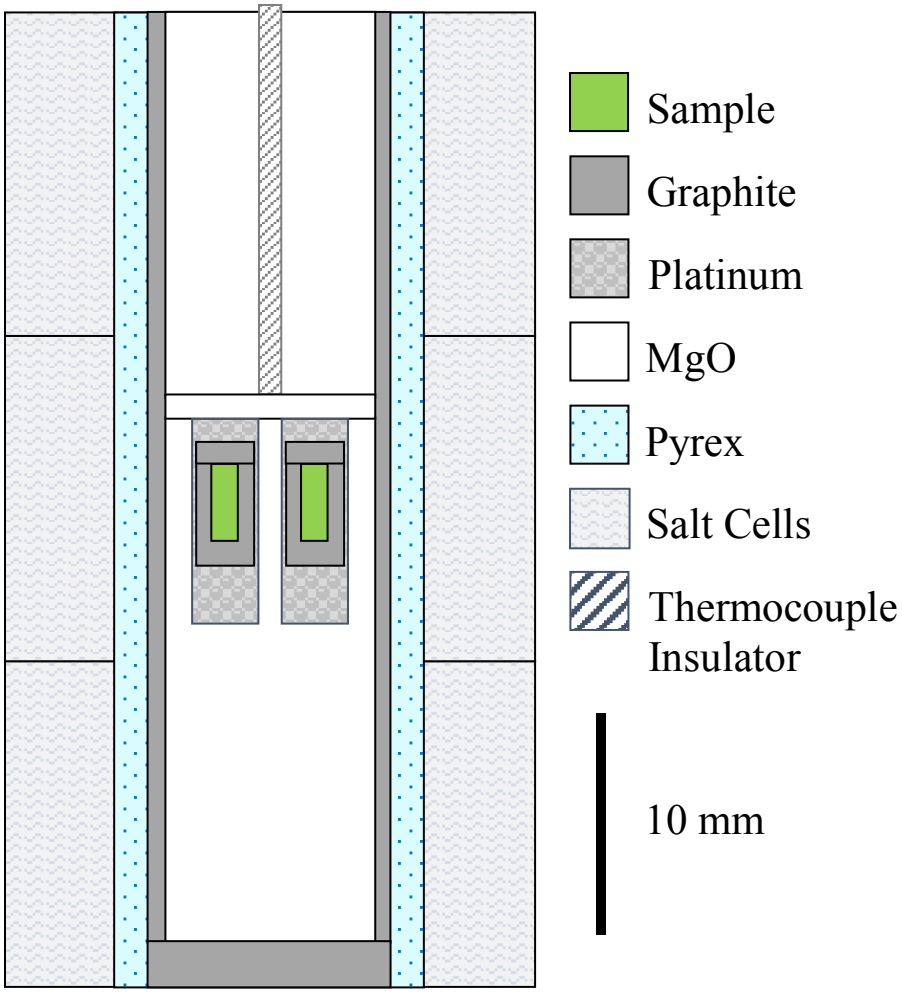

Figure 3. Scale diagram of a typical 1.905 mm experimental assembly. Thermocouple wires are not shown but pass through the thermocouple insulator and joined at its lower extremity.

3.3 Control of oxygen fugacity

As previously discussed, oxygen fugacity exerts a strong influence on chromium solubility and is therefore an important parameter to control in experiments (Murck and Campbell 1986; Roeder and Reynolds 1991). Samples were buffered internally by the graphite crucible, which with the use of fully-oxidised starting materials, buffers the fO_2 near the C-CO equilibrium. To check the fO_2 of experiments, a small piece of Pt wire was added within the graphite crucible in selected runs. The Pt wire records the oxygen fugacity through the equilibrium:

$$Fe + \frac{1}{2}O_2 \Leftrightarrow FeO \qquad (2)$$

with the equilibrium constant:

$$K_{eq} = \frac{a_{FeO}^{oxide}}{a_{Fe}^{metal}} \bullet fO_2 \frac{1}{2} \quad (3)$$

in which the a_{FeO}^{oxide} and a_{Fe}^{metal} are the activities of FeO and Fe in the oxide and metal phases, respectively. The oxygen fugacity can be determined through the relation:

$$lnK_{eq} = lna_{FeO}^{oxide} - lna_{Fe}^{melt} - \frac{1}{2}\ln fO_2 \quad (4)$$

Recognizing also that:

$$-RTlnK_{eq} = \Delta G^{\circ}{}_{1,T} + (P-1)\Delta V \quad (5)$$

$$= -\frac{\Delta G^{\circ}{}_{1,T}}{RT} - \frac{(P-1)\Delta V}{RT} \quad (6)$$

Substituting (6) in (4) and solving for $lnfO_2$ yields:

$$\ln fO_2 = 2\left[lna_{FeO}^{oxide} - lna_{Fe}^{metal} + \frac{\Delta G^{\circ}{}_{1,T}}{RT} + \frac{(P-1)\Delta V}{RT}\right] \quad (7)$$

Values of $\Delta G^{\circ}{}_{1,T}$ are calculated from equation (9) in Holzheid et al. (1997) and ΔV from the molar volume data of ?? The activity of FeO in the oxide phase (in this case silicate melt) is assumed to follow the approximation $a_{FeO}^{oxide} = 1.7 \bullet X_{FeO}^{oxide}$, and a_{Fe}^{metal} is calculated from the activity-composition relations described in Medard *et al.* (2008).

Chapter 4: Analytical Methods

4.1 Sample preparation

Whole capsules were set in 1" epoxy pucks, then ground with 320 grit SiC, then 400 grit SiC, and 600 grit SiC to expose their contents in lengthwise cross-section. To minimize plucking and loss of the run products during the polishing process, the exposed contents were then impregnated with epoxy and again allowed to set. Excess epoxy was removed with 600 grit SiC and the sample polished with 1 μm, then 0.3 μm alumina. The samples were carbon-coated after polishing and prior to analysis by electron microprobe.

4.2 Electron microprobe analysis

Run products were analysed at the Robert M. MacKay Electron Microprobe Laboratory at Dalhousie University. Major element compositions were determined using the JEOL JXA-8200 Electron Probe Micro-Analyser (EMPA). All analyses were done using a 15 kV accelerating voltage and 20 nA beam. Chromites were analysed using a focused 1 μm beam and silicate glasses were analysed with a 10 μm defocused beam. The texturally complex quenched run products produced in hydrous experiments were analysed with a 30 μm beam to determine an average composition incorporating both quench dendrites and interstitial glass. Silicate glasses were measured against the following standards: natural basalt (Si, Ca, Al, Fe, Mg), bustamite (Mn), albite (Na), titanium oxide (Ti), chromium oxide (Cr), and sanidine (K). Data reduction was performed off-line using the ZAF (atomic number-absorption-fluorescence) model to correct for matrix effects.

4.3 Laser ablation inductively-coupled plasma mass spectrometry analysis

Chromium and trace element concentrations were measured at the Health and Environments Research Centre (HERC) at Dalhousie University, using the DalLAIS laser-ablation ICP-MS. Sample ablation is achieved using a 213 nm frequency quintupled Nd:YAG laser in tandem with a Thermo Scientific iCAP Q ICP-MS quadrupole mass spectrometer. The ablation cell is flushed with He to improve sensitivity (Eggins *et al.* 1998). A laser repetition rate of 5 Hz and a spot size of 25 μm was used to analyse silicate glasses. Individual analyses were collected using the factory-supplied time resolved software. Analyses were done in three parts, with the first 20 seconds dedicated to background acquisition while the ablation cell was flushed

with He, then 60 seconds of laser ablation, followed by 60 seconds of cell washout. Wherever possible, 4 analyses were made on each sample. Data reduction was done off-line, using the Iolite version 3.6 software package. V, Cr, Mn, Ni, and Cu were quantified against the SRM NIST 610 glass, for which Iolite uses the reference values of 442 ± 86 $\mu g g^{-1}$ V, 405 ± 64 $\mu g g^{-1}$ Cr, 485 ± 10 $\mu g g^{-1}$ Mn, 458.7 ± 4 $\mu g g^{-1}$ Ni, and 430 ± 48 $\mu g g^{-1}$ Cu. Ca concentrations, as measured by electron microprobe analyses, were used to correct ablation yields.

Chapter 5: Results

5.1 Modelling results

Saturation curves were produced using the rhyolite-MELTS and SpinMelt-2 software packages described previously. Superimposing the model curves reveals that the addition of ~3.5 wt% H_2O at 1400°C could induce chromite to appear as the sole liquidus phase.

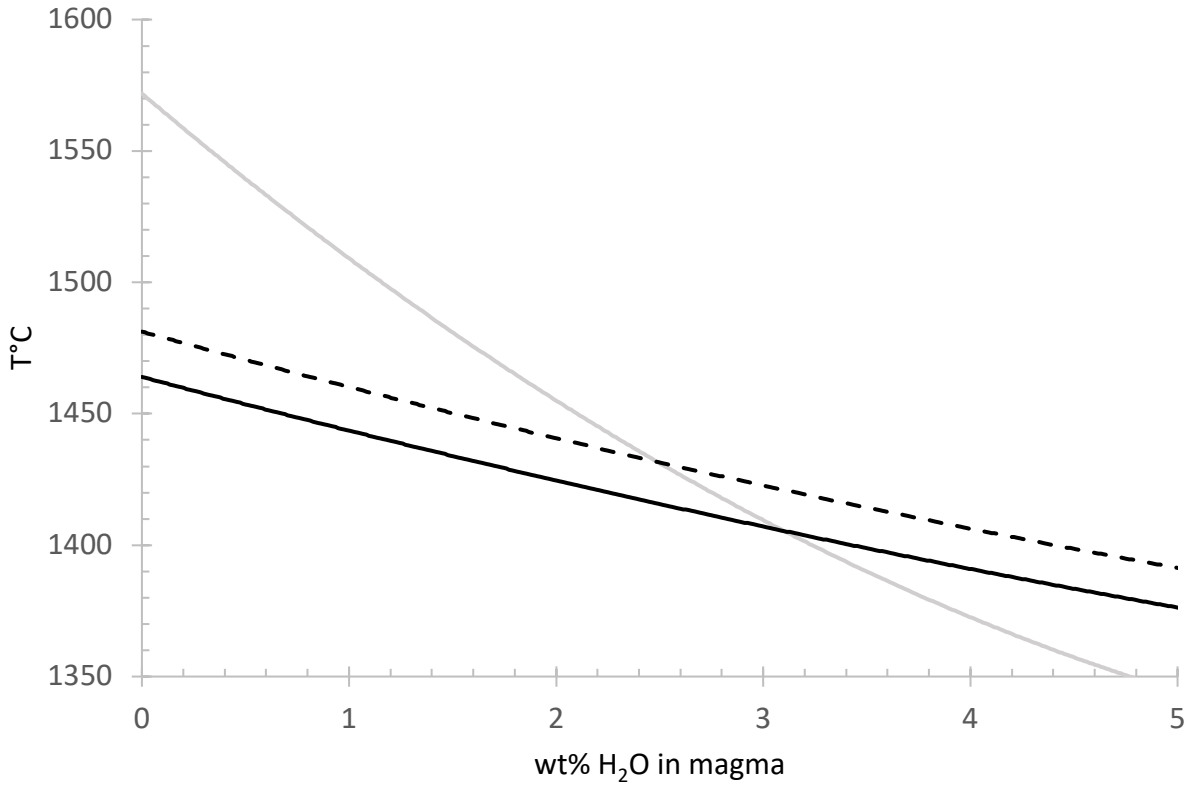

Figure 4. Saturation curves for olivine and chromite, calculated using rhyolite-MELTS (Gualda *et al.* 2012; Ghiorso and Gualda 2015) and SpinMelt-2 (Nikolaev *et al.* 2018a; Nikolaev *et al.* 2018b) projected onto T, wt% H_2O plane. Chromite-in calculated for both FMQ (dashed) and FMQ-1.2 (solid) fO_2 conditions. The order of crystallization is calculated to shift from olivine-chromite to chromite-olivine at between 2.5 and 3.5 wt% H_2O.

5.2 Run Products

There was considerable textural heterogeneity, both among the different experiments and within them. In some cases, melt (glass) was interspersed with fine, skeletal quench crystals,

which were obstacles to the glass analyses. Spatial variation in the glass and quench textures was most pronounced in the initial experiments with the longest (8 mm) crucible bore, shown in Figure 5, but was not appreciable in experiments done using the shortest (3.5 mm) bore length.

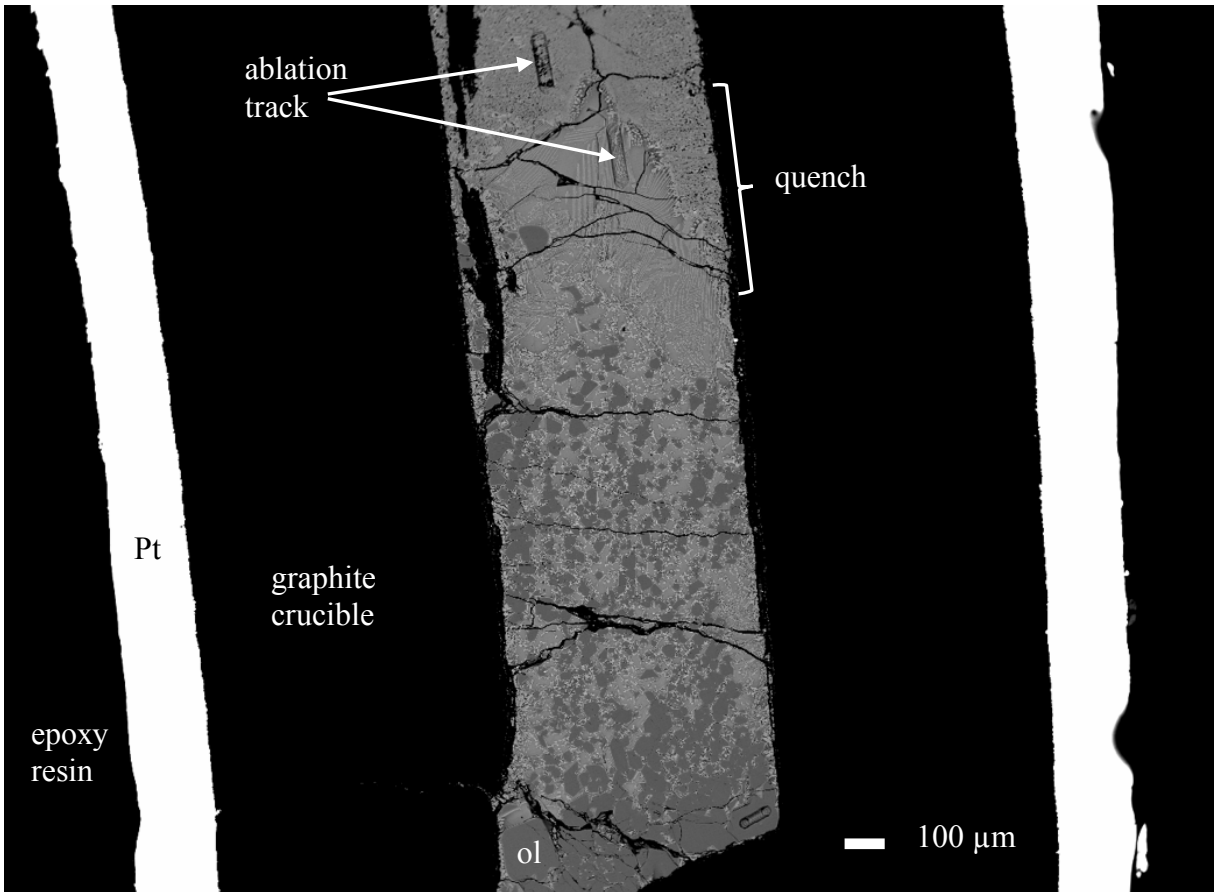

Figure 5. This back-scattered electron (BSE) image of experiment KW0-2 (8 mm bore length) illustrates the textural diversity of run products. This sample shows a layer of euhedral olivine at the base, followed upwards by a region dominated by a fine-scale intergrowth of quench dendrites of clinopyroxene.

Olivine was present in all run products at 1350°C and 1400°C, and in anhydrous experiments run at 1450°C. At 1600°C, only glass is present, and at 1550°C only a small, anhedral, skeletal quench product is observed. The liquidus temperature of the anhydrous compositions is above 1450°C, but below 1550°C.

Of the hydrous experiments, only KW3-1, with ~9200 ppm in the starting composition, crystallized chromite. In all cases where chromite was observed as an equilibrium phase, it appeared as small (<5 μm), usually disseminated, euhedral crystals.

Equilibrium olivine was euhedral and varied in size from 5-20 μm in anhydrous experiments (Figure 6a) to several tens of microns at high water contents (Figure 6c). Olivine was frequently rimmed by quench pyroxene, nearly indistinguishable in reflected light but easily identified in back-scattered electron (BSE) images (Figure 5, Figure 6). Mineral identities were confirmed semi-quantitatively using the energy dispersive spectra (EDS) software on-line during EMPA.

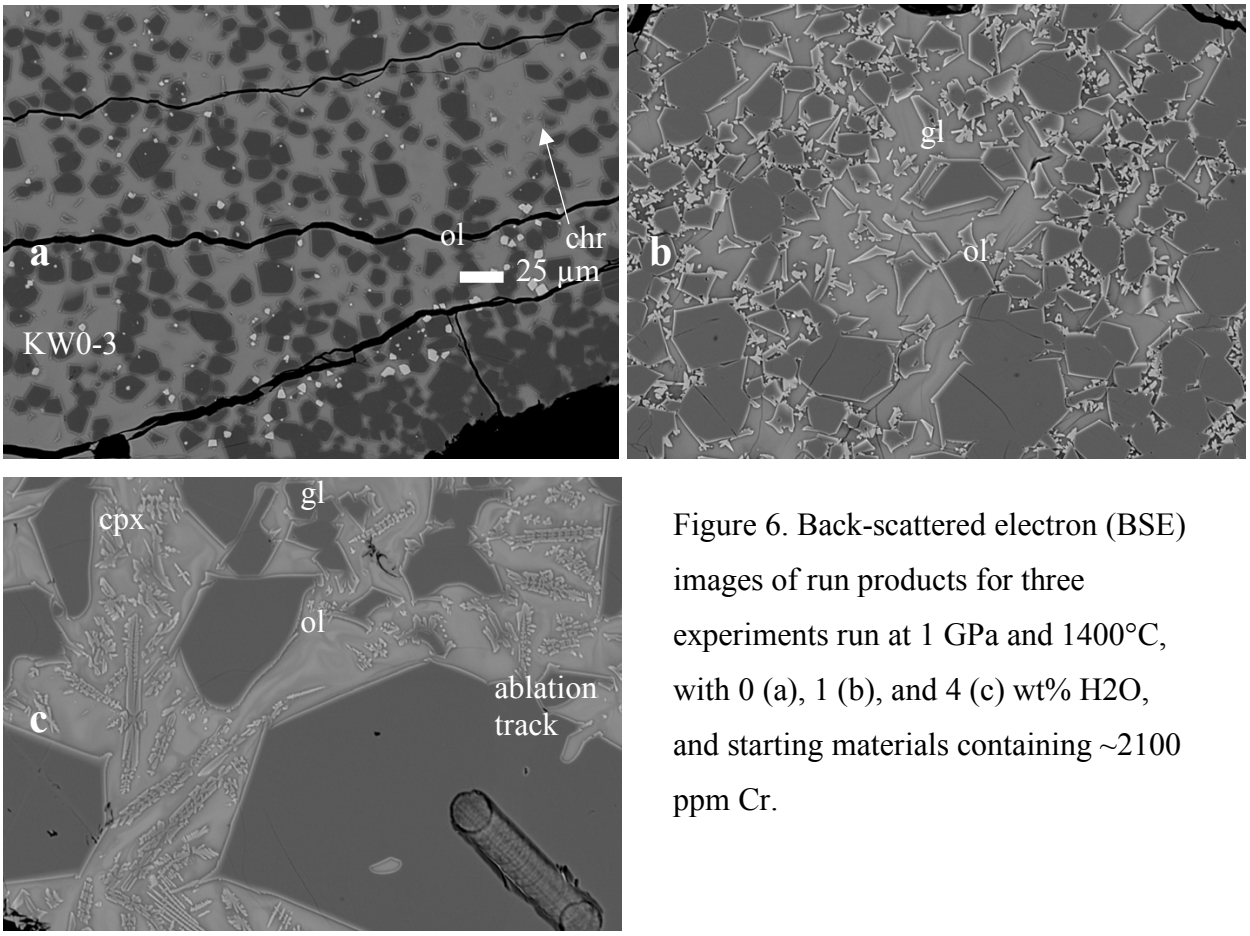

Figure 6. Back-scattered electron (BSE) images of run products for three experiments run at 1 GPa and 1400°C, with 0 (a), 1 (b), and 4 (c) wt% H2O, and starting materials containing ~2100 ppm Cr.

Successful experiments were those in which the run products were compositionally homogeneous and there was no evidence of water loss. Water contents of the glasses were confirmed approximately by appropriately low EMPA totals (Figure 7). Where noted, fine

textures were analysed with a more widely defocused beam (30 µm) and represent average compositions of the anhydrous quenched material and hydrous interstitial glass.

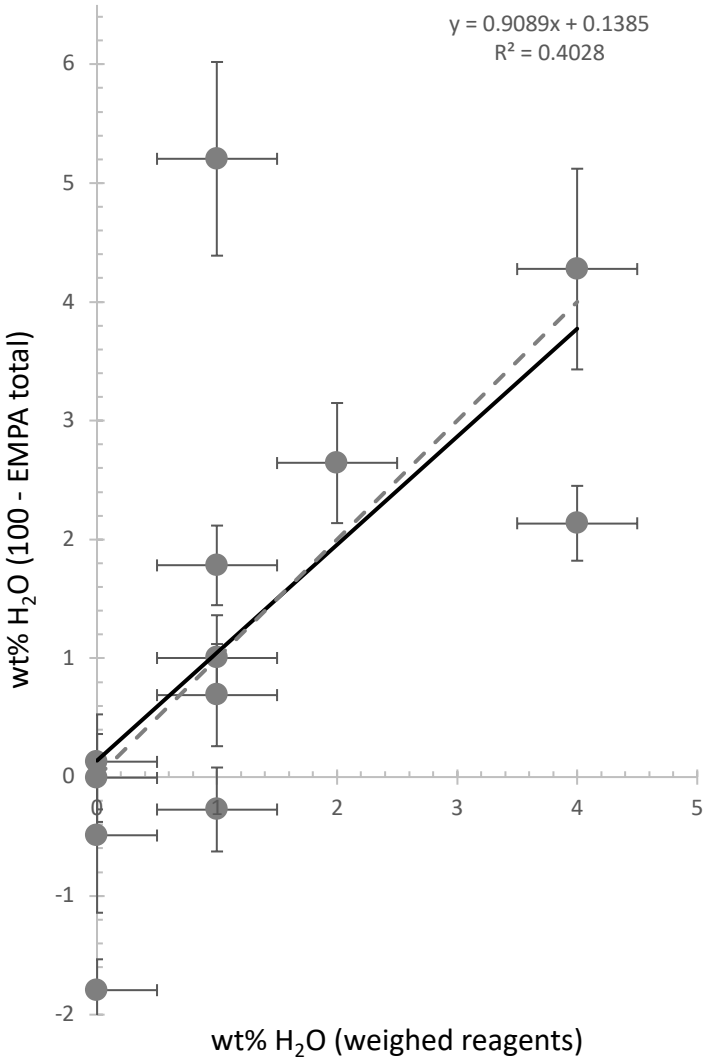

Figure 7. Diagram illustrating the agreement between EMPA total deficits and the weighed amount of H_2O added to the experimental starting material. Deficits were calculated based on fO_2-corrected EMPA totals. A slope of 1 (dashed trendline) would indicate perfect agreement between the measured and weighed values; most of the plot within error of this trend. The best-fit line for this data set is shown in solid black.

Table 2. Summary of experiments

Experiment	T°C	wt% H2O	SM ppm Cr	Melt Cr (ppm)	Phases
KW0-1	1400	0	2100	2567	ol + chr + liq
KW0-2	1400	1	2100	3363	ol + liq
KW0-3	1400	4	2100	3264	ol + liq
KW1-1	1350	1	2100	3330	ol + liq
KW1-2	1350	2	2100	3227	ol + liq
KW1-3	1350	4	2100	3565	ol + liq
KW2-1	1400	0	9200	2952	ol + chr + liq
KW2-2	1400	0	4600	3340	ol + chr + liq
KW2-3	1400	0	2300	2980	ol + chr + liq
KW3-1	1450	1	9200	5795	chr + liq
KW3-2	1450	1	4600	5035	liq
KW3-3	1450	1	2300	3418	ol + liq
KW4-1	1390	1	2300	3312*	ol + liq
KW6-1	1450	0	2300	3774*	ol + liq
KW5-1	1400	0.5	3400	~3300	ol + liq
KW5-2	1400	1	3400	~3200	ol + liq
KW5-3	1400	2	3400	~4100	ol + liq
KW7-1	1600	0	4800	no data	liq
KW7-1	1550	0	4800	no data	liq

* experiments for which there are not yet EMPA major element data; Cr concentrations calculated using Iolite use the average Ca contents measured in melts produced at the same temperature conditions.

Table 3. Summary of melt compositions (major elements, EMPA)

Exp	SiO_2	TiO_2	Al_2O_3	FeO	Cr_2O_3	MnO	MgO	CaO	Na_2O	K_2O	Tot
KW0-1	47.03	0.73	14.26	12.18	0.30	0.24	10.37	14.70	0.79	1.08	101.67
1σ	0.30	0.05	0.95	0.53	0.04	0.02	1.56	0.67	0.06	0.10	0.26
KW0-2	49.23	0.79	15.81	8.47	0.31	0.21	3.32	15.04	0.48	1.04	94.17
1σ	1.00	0.09	1.84	0.11	0.02	0.01	6.80	1.51	0.06	0.04	0.82
KW0-3	50.38	.80	15.30	9.26	0.32	0.21	4.55	15.07	0.70	1.16	97.76
1σ	0.39	0.04	1.02	0.58	0.03	0.03	1.23	0.30	0.03	0.14	0.32

KW1-1	48.70	0.73	13.74	10.33	0.35	0.23	5.99	14.48	0.75	1.05	96.35
1σ	0.53	0.0.3	0.91	0.75	0.03	0.03	1.13	0.30	0.08	0.17	0.24
KW1-2	48.87	0.76	14.12	9.67	0.33	0.24	5.11	14.79	0.78	1.10	95.76
1σ	0.26	0.03	0.42	0.33	0.03	0.03	0.59	0.23	0.05	0.06	0.29
KW1-3	47.87	0.79	14.85	8.59	0.29	0.22	4.12	15.40	0.81	1.19	94.13
1σ	0.35	0.03	0.36	0.47	0.04	0.02	0.42	0.20	0.04	0.06	0.31
KW2-1	46.63	0.65	12.51	12.23	0.39	0.23	12.73	12.46	0.81	1.11	99.75
1σ	0.26	0.03	0.40	0.13	0.04	0.02	1.32	0.58	0.04	0.05	0.40
KW2-2	46.50	0.63	11.96	12.43	0.43	0.22	13.63	12.11	0.88	1.10	99.89
1σ	0.29	0.07	0.70	0.31	0.05	0.01	2.01	0.86	0.08	0.10	0.37
KW2-3	46.56	0.60	11.56	12.70	0.43	0.22	14.53	11.82	0.83	1.12	100.37
1σ	0.29	0.07	0.70	0.31	0.05	0.01	2.01	0.86	0.08	0.10	0.65
KW3-1[a]	45.31	0.45	9.36	13.04	0.82	0.23	20.70	8.93	0.55	0.78	100.16
1σ	0.60	0.04	0.59	0.59	0.03	0.03	1.12	0.59	0.05	0.11	0.35
KW3-2[a]	45.07	0.44	9,35	12.77	0.70	0.23	20.62	8.60	0.56	0.86	100.17
1σ	0.34	0.03	0.28	0.09	0.03	0.02	0.64	0.31	0.04	0.04	0.43
KW3-3[a]	45.21	0.45	9.46	12.68	0.50	0.24	20.11	8.74	0.65	0.86	98.89
1σ	0.31	0.03	0.31	0.22	0.03	0.03	0.87	0.60	0.07	0.07	0.36

a. Quench analyses performed using a 30 μm defocused beam.

Table 4. Trace element concentrations (ppm) in melt (LA-ICP-MS)

Exp	V51	Cr52	Cr53	Mn55	Ni61	Cu63	Cu65
KW1-1	13.38	3330.25	3160.00	2952	7.56	0.47	0.84
1σ	0.18	50.25	58.00	66.75	1.04	0.05	0.09
KW1-2	25.36	3226.75	3160.25	3053.50	6.36	0.65	0.94
1σ	0.31	53.50	64.25	79.00	1.04	0.08	0.13
KW1-3	24.66	3564.50	3423.75	3367.00	7.40	0.46	0.87
1σ	0.29	50.25	57.50	69.00	1.15	0.06	0.11

KW2-1	13.21	2951.50	2920.75	2262.25	6.20	1.33	1.65
1σ	0.22	55.00	74.75	75.25	1.18	0.23	0.29
KW2-2[b]	2.21	3339.67	3261.67	2237.67	5.22	0.29	0.51
1σ	0.07	52.67	65.67	58.33	1.01	0.05	0.10
KW2-3	2.21	2979.50	2949.50	1828.00	3.89	0.28	0.44
1σ	0.08	41.25	56.50	43.25	1.05	0.06	0.12
KW3-1	7.15	5794.75	5475.75	1810.25	3.95	1.33	1.46
1σ	0.13	82.25	102.25	42.00	0.88	0.17	0.19
KW3-2	4.28	5034.75	4730.00	1811.00	3.35	0.95	1.27
1σ	0.10	77.25	90.25	40.50	0.83	0.12	0.19
KW3-3	7.28	3417.50	3382.50	1904.75	3.10	1.91	2.12
1σ	0.14	45.00	60.25	41.00	0.89	0.22	0.25
KW4-1[c]	8.38	3311.64	3217.52	1812.47	2.70	0.18	0.42
1σ	0.22	66.50	87.00	60.50	1.13	0.07	0.14
KW5-1[b,c]	13.55	3352.72	3301.00	2097.51	2.68	0.36	0.57
1σ	0.59	142.75	175.00	135.00	1.77	0.11	0.35
KW5-2[b,c]	12.05	3206.21	3189.58	1902.77	3.82	0.35	0.63
1σ	0.32	100.00	130.00	88.50	1.40	0.09	0.17
KW5-3[b,c]	7.40	4170.73	4150.78	2141.91	16.43	10.36	12.05
1σ	1.65	300.00	305.00	205.00	29.15	4.07	10.81
KW6-1[c]	3.11	3774.20	3750.46	2215.98	3.17	<0.21	0.40
1σ	0.11	60.25	82.00	61.50	1.18		0.15

Reference	V51	Cr52	Cr53	Mn55	Ni61	Cu63	Cu65
BHVO1	309.85	282.13	282.08	1439.67	135.80	133.90	135.30
1σ	2.60	2.49	3.00	14.43	5.17	1.41	1.44
BIR1	308.20	388.05	384.48	1506.83	178.08	116.07	117.52
1σ	2.97	4.15	4.45	16.83	4.77	1.33	1.43

Accepted values (Jochum et al. 2016)

BHVO1	313.8	287.6	287.6	not given	120	137.2	137.2
BIR	320.6	392.9	392.9	not given	168.9	120.7	120.7

b. Samples analysed with fewer than 4 laser spots due to spatial constraints.

c. Experiments that have not yet been measured by EMPA; concentrations calculated in Iolite using CaO wt% of melt measured for experiments run at same temperature conditions.

5.3 Spinel compositions

The Cr_2O_3 content of the spinel varies systematically with the $FeCr_2O_4$ content of the starting material and is inversely correlated with Al_2O_3.

Table 5. Chromite compositions

Exp	SiO_2	TiO_2	Al_2O_3	FeO	Fe_2O_3	Cr_2O_3	MnO	MgO	CaO	Tot
KW0-1	0.29	0.25	34.72	13.85	-	30.74	0.22	17.32	0.23	97.61
1σ, n=13	0.07	0.02	0.42	0.12	-	0.69	0.02	0.23	0.11	0.78
KW2-1	0.27	0.28	26.84	14.83	-	38.90	0.23	15.88	0.25	97.46
1σ, n=11	0.08	0.02	0.66	0.23	-	0.80	0.02	0.25	0.08	0.44
KW2-2	0.29	0.31	26.28	14.55	-	39.36	0.23	16.13	0.22	97.36
1σ, n=5	0.04	0.01	0.93	0.15	-	1.50	0.02	0.32	0.05	0.57
KW2-3	0.27	0.31	23.79	15.39	-	42.24	0.23	15.43	0.23	97.88
1σ, n=6	0.04	0.02	0.70	0.15	-	0.74	0.02	0.14	0.07	0.38
KW3-1	0.27	0.27	14.83	13.42	-	53.57	0.24	15.26	0.21	98.06
1σ, n=7	0.02	0.03	0.31	0.21	-	0.41	0.02	0.10	0.04	0.72

Chapter 6: Discussion

6.1 Chromium solubility as a function of H_2O content of the melt

Although the effect of water on Cr solubility has not yet been quantified, at 1400°C, chromite disappeared from the stable assemblage with the addition of water. It is clear even from these few data that water exerts some control on the activity of Cr in the melt, observed in an increase in solubility and hence a decrease in the chromite liquidus. Figure # shows a schematic representation of the quantitative data available at this time. At 1400°C and for anhydrous compositions, the minimum Cr content of the glass at chromite saturation is ~2600 ppm. The addition of water suppressed chromite saturation even with as much as ~3300 ppm Cr in the melt.

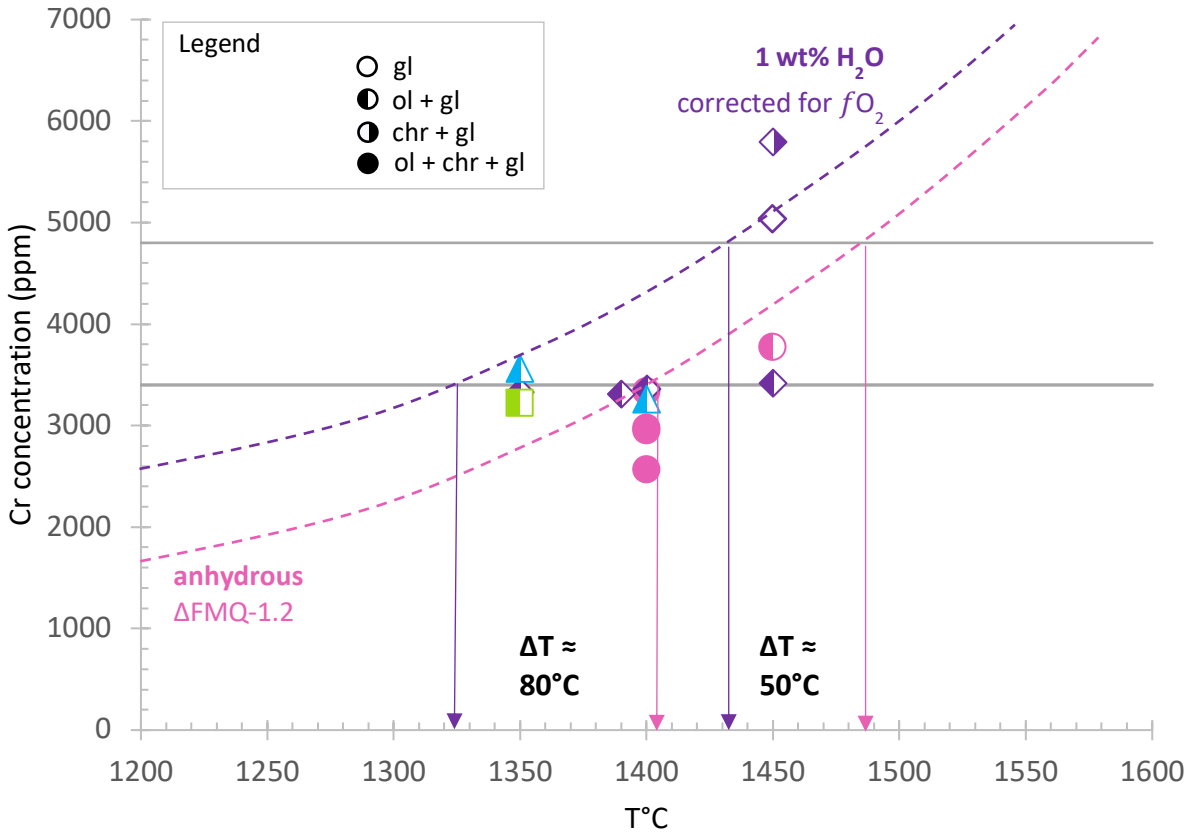

Figure 8. Estimated chromite saturation curves in komatiite at 1 GPa. The 1 wt% H_2O curve is corrected for an estimated shift in fO_2 to 0.5 log units below C-CO with the addition of water to the composition. For a komatiite with ~4800 ppm Cr at the C-CO buffer, the addition of 1 wt%

H_2O causes a ~50°C depression in the chromite-in temperature. For a komatiite with ~3400 ppm Cr, the addition of 1 wt% H_2O causes a ~80°C depression in the chromite-in temperature.

6.2 Effect of H_2O on fO_2 in experimental assembly

It is clear from these experiments that the chromite liquidus is suppressed by the addition of water to a melt contained in a graphite-lined Pt capsule. However, it is important to address possible confounding factors. Firstly, it is possible that the addition of water may affect the buffering capacity of the graphite lining. It will be necessary to constrain the effects of H_2O on fO_2 in these experiments in order to quantify the impact of water on Cr solubility. Since Cr solubility is inversely related to fO_2, if the additional hydrogen introduced by H_2O imposes a lower fO_2 than that of the anhydrous experiment at otherwise equivalent conditions, this would result in an increase in the solubility of Cr that could be misconstrued as a water effect. A reduction in fO_2 by even just 0.5 log units from the C-CO buffer could account for up to ~700 ppm of increased solubility at 1400°C (Figure 9, after Roeder and Reynolds).

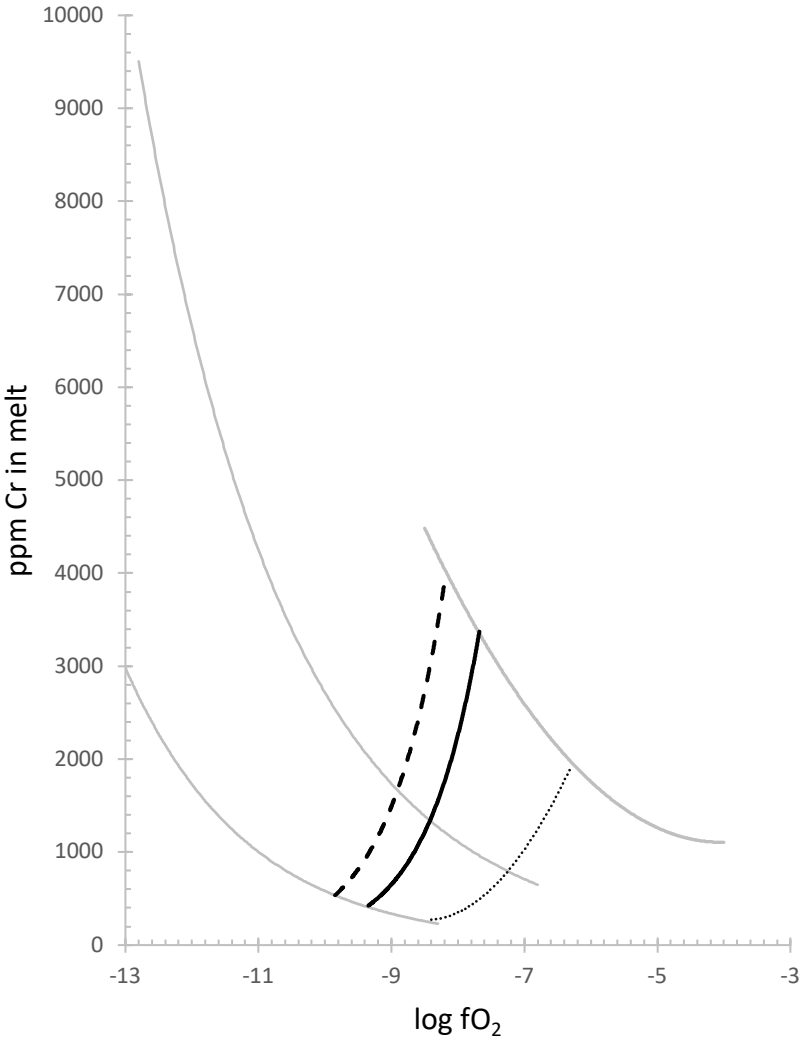

Figure 9. Chromite saturation curves as a function of fO_2 (after Roeder and Reynolds 1991). Curves are shown for FMQ (dotted), C-CO (solid), and C-CO-1.2 (dashed), illustrating the effect of fO_2 on Cr solubility.

6.3 Effect of H_2O on melt structure

The activity of chromite in either the oxide or melt phase can be expressed by the relation

$$a_i = X_i \gamma_i \qquad \text{(equation 8)}$$

where a is the activity of component i; X is the mole fraction; and γ is the activity coefficient. At chromite saturation, the activity a = 1. The activity coefficient γ is then directly proportional to the concentration, and therefore changes in chromite solubility should reflect changes in γ_i in the mineral or melt phase. If the Cr content of the glass at chromite saturation is greater with the addition of water, then the activity coefficient is reduced.

Supposing that the effect of water on fO_2 in the experiment is negligible (<0.1 log units), the the observed reduction in chromite solubility must reflect changes in γ_i. As described above, Cr has a strong octahedral site preference. This is true not only in a crystalline phase, but also in a molten silicate (Berry *et al.* 2004). Whereas only Cr^{3+} enters the spinel structure, it may be that the observed increase in Cr solubility with the addition of water is a result of the effect of water on the capacity of the melt to accommodate Cr^{3+}. Water acts as a network-modifier in silicate melts by disrupting silica tetrahedra to form Si-OH- (CITE?). This increases the electron density and therefore the ability of the melt to accommodate both the site preference and charge of Cr^{3+}.

6.3 Phase relations

With the exception of KW3-1, which contained ~9200 ppm Cr, olivine is the first phase to crystallize at any of the conditions explored in this study. It is likely that the suppression of olivine crystallization indirectly impacts the chromite liquidus. Whereas it is the crystallization of olivine, in which Cr is incompatible, that enriches the melt in Cr to the point of chromite saturation, if olivine growth is suppressed, then so too is that of chromite. In the low-Cr (~2100 ppm) experimental compositions, chromite cannot be induced to crystallize as the sole liquidus phase. Natural komatiites, even those borne of the most reducing conditions reasonable for Earth, can dissolve a maximum of a few thousand ppm of Cr before saturating in chromite (Barnes 1998).

6.4 Geological implications

Komatiites have been estimated to contain as much as 0.5 (Green et al. 1975) to 6 wt% H_2O (Grove and Parman 2004) on emplacement. If the experimental results shown here are a true indication that Cr solubility is increased by the presence of water, then there are implications for Cr transfer by komatiitic melts. If the melt conditions facilitate a relatively high capacity for

dissolved Cr, then the chromite that eventually precipitates from such a melt may be of higher Cr content and thus higher economic value, as evidenced here.

The results of this study improve our understanding of at least one possible mechanism of chromite-only deposition. The presence of water in the melt at the temperatures at which komatiites are estimated to have been emplaced (Grove and Parman 2004) could induce a reversal in the silicate-spinel crystallization order and increase the temperature interval over which chromite may precipitate, allowing it to accumulate in the monomineralic deposits observed in nature. Conduit-hosted deposits like the one that inspired this study are likely to have been injected into dynamic and irregular conditions, which may explain some of the variability in the types of chromite crystallization that occur, and the switch between disseminated accessory chromite and cumulus deposits.

Chapter 7: Future Work

With the methodology now finely-tuned, the opportunity to define the relationship between H_2O and chromite solubility is within reach. Future work will require a two-part approach, with the first involving a series of chromite-added experiments to ensure chromite saturation at run conditions. Then, the Cr content of the glasses at chromite saturation will be measured to establish the effect that water may have on Cr solubility. The second part will examine the phase relations in a komatiite with a geologically reasonable Cr content, as guided by the interpretations of Barnes (1998).

In order to establish a robust trend in Cr solubility with respect to magmatic water, the melt must be saturated in chromite over a range of water contents. Chromite saturation in experimental runs can be ensured by adding sufficient Cr_2O_3 and Fe_2O_3 to the starting composition in the form of powdered oxides (Roeder and Reynolds 1991). This methodology does not necessarily reflect geologically reasonable conditions; whereas the melt is supersaturated in chromite, chromite will always appear as a liquidus phase. This is important to note as these types of experiments cannot be used directly to determine the crystallization temperature of chromite relative to olivine. They are, however, and efficient means of addressing the Cr solubility problem.

At the time of writing, a series of experiments is underway using a ~4800 ppm Cr komatiite starting material. While higher in Cr than the global average at FMQ, this composition was chosen to compensate for the increased solubility of Cr at the fO_2 of the C-CO buffer, which is approximately ΔFMQ-1.2 at the temperature range explored in these experiments. Present and future experiments with Pt wire fO_2 sensors will be analysed to confirm these conditions.

References

Theses and Dissertations

Azar, B. 2010. The Blackbird chromite deposit, James Bay Lowlands of Ontario, Canada: implications for chromitite genesis in ultramafic conduits and open magmatic systems. M.Sc. thesis, Department of Geology, The University of Toronto, Toronto, O.N.

Journal Articles

Arndt, N.T. 1977. Thick, layered peridotite-gabbro lava flows in Munro Township, Ontario. Canadian Journal of Earth Sciences, 14: 2620-2637.

Arndt, N.T. 2003. Komatiites, kimberlites, and boninites. Journal of Geophysical Research, 108(B6): 2293.

Arndt, N.T., Naldrett, A.J., Pyke, D.R. 1977. Komatiitic and iron-rich tholeiitic lavas of Munro Township, northeast Ontario. Journal of Petrology, 18(2): 319-69.

Arndt, N.T., Francis, D., Hynes, A.J. 1979. The field characteristics and petrology of Archean and Proterozoic komatiites. Canadian Mineralogist, 17: 147-163.

Arndt, N., Ginibre, C., Chauvel, C., Albarède, F., Cheadle, M., Herzberg, C., Jenner, G., Lahaye, Y. 1998. Were komatiites wet? Geology, 8: 739-742.

Barnes, S.J. 1986. The distribution of chromium among orthopyroxene, spinel and silicate liquid at atmospheric pressure. Geochimica et Cosmochimica Acta, 50: 1889-1909.

Barnes, S.J. 1998. Chromite in komatiites, I. Magmatic controls on crystallization and composition. Journal of Petrology, 39(10): 1689-1720.

Bouquain, S., Arndt, N., Faure, F., Libourel, G. 2014. An experimental study of pyroxene crystallization during rapid cooling in a thermal gradient: application to komatiites. Solid Earth, 5: 641-650.

Christyakova, S., Latypov, R., Zaccarini, F. 2015. Chromitite dykes in the Monchegorsk Layered Intrusion, Russia: in situ crystallization from chromite-saturated magma flowing in conduits. Journal of Petrology, 56(12): 2395-2424.

Eggins, S.M., Kinsley, L.P.J., Shelley, J.M.M. 1998. Depositon and element fractionation processes during atmospheric pressure laser sampling for analysis by ICPMS. Applied Surface Science, 127: 278-286.

Faure, F., Arndt, N., Libourel, G. 2006. Formation of spinifex texture in komatiites: an experimental study. Journal of Petrology, 47(9): 1591-1610.

Fiorentini, M.L., Beresford, S.W., Stone, W.E., Deloule, E. 2012. Evidence of water degassing during emplacement and crystallization of 2.7 Ga komatiites from the Agnew-Wiluna greenstone belt, Western Australia. Contributions to Mineralogy and Petrology, 164: 143-155.

Ghiorso, M.S., Sack, R.O. 1995. Chemical mass transfer in magmatic processes IV. A revised and internally consistent thermodynamic model for the interpolation and extrapolation of liquid-solid equilibria in magmatic systems at elevated temperatures and pressures. Contributions to Mineralogy and Petrology, 119: 197-212.

Ghiorso, M.S., Gualda, G.A.R. 2015. An H_2O-CO_2 mixed fluid saturation model compatible with rhyolite-MELTS. Contributions to Mineralogy and Petrology, 169(6): 53.

Green, D.H., Hibberson, W.O., Rosenthal, A., Kovács, I., Yaxley, G.M., Falloon, T.J., Brink, F. 2014. Experimental study of the influence of water on melting and phase assemblages in the upper mantle. Journal of Petrology, 55(10): 2067-2096.

Grove, T.L., Parman, S.W. 2004. Thermal evolution of the Earth as recorded by komatiites. Earth and Planetary Science Letters, 219: 173-187.

Gualda, G.A.R., Ghiorso, M.S., Lemons, R.V., Carley, T.L. 2012. Rhyolite-MELTS: a modified calibration of MELTS optimized for silica-rich, fluid-bearing magmatic systems. Journal of Petrology, 53: 875-890.

Holzheid, A., Palme, H., Chakraborty, S. 1997. The activities of NiO, CoO and FeO in silicate melts. Chemical Geology, 139: 21-38.

Irvine, T.N. 1975. Crystallization sequences in the Muskox intrusion and other layered intrusions–II. Origin of chromitite layers and similar deposits of other magmatic ores. Geochimica et Cosmochimica Acta, 39: 991-1020.

Irvine, T.N. 1977. Origin of chromitite layers in the Muskox intrusion and other stratiform intrusions: a new interpretation. Geology, 5: 273-277.

Jochum, K.P., Weis, U., Schwager, B., Stoll, B., Wilson, S.A., Haug, G.H., Andreae, M.O., Enzweiler, J. 2016. Reference values following ISO guidelines for frequently requested rock reference materials. Geostandards and Geoanalytical Research, 40(3): 333-350.

Kinzler, R.J., Grove, T.L. 1985. Crystallization and differentiation of Archean komatiite lavas from northeast Ontario: phase equilibrium and kinetic studies. American Mineralogist, 70: 40-51.

Lipin, B.R. 1993. Pressure increases, the formation of chromite seams, and the development of the ultramafic series in the Stillwater Complex, Montana. Journal of Petrology, 34(5): 955-976.

Mungall, J.E., Harvey, J.D., Balch, S.J., Azar, B., Atkinson, J., Hamilton, M. 2010. Chapter 28: Eagle's Nest: a magmatic Ni-sulfide deposit in the James Bay Lowlands, Ontario, Canada. Society of Economic Geologists, Special Publication, 15: 539-557.

Mungall, J.E., Kamo, S.L., McQuade, S. 2016. U-Pb geochronology documents out-of-sequence emplacement of ultramafic layers in the Bushveld Igneous Complex of South Africa. Nature Communications, 7: 13385.

Murck, B.W., Campbell, I.H. 1986. The effects of temperature, oxygen fugacity and melt composition on the behaviour of chromium in basic and ultrabasic melts. Geochimica et Cosmochimica Acta, 50: 1871-1887.

Nesbitt, R.W., Sun, S-S., Purvis, A.C. 1979. Komatiites: geochemistry and genesis. Canadian Mineralogist, 17: 165-186.

Nicholson, D.M., Mathez, E.A. 1990. Petrogenesis of the Merensky Reef in the Rustenburg section of the Bushveld Complex. Contributions to Mineralogy and Petrology, 107: 293-309.

Nikolaev, G.S., Ariskin, A.A., Barmina, G.S. 2018a. SPINMELT-2.0: Simulation of spinel-melt equilibrium in basaltic systems under pressures up to 15 kbar: I. Model formulation, calibration, and tests. Geochemistry International. Russian Federation: Russian Federation 56: 24-45.

Nikolaev, G.S., Ariskin, A.A., Barmina, G.S. 2018b. SPINMELT-2.0: Simulation of spinel-melt equilibrium in basaltic systems under pressures up to 15 kbar: II. Description of the program package, the topology of Cr-spinel-melt model system, and petrological implications. Geochemistry International, Russian Federation: Russian Federation, 56: 125-135.

Parman, S.W., Dann, J.C., Grove, T.L., de Wit, M.J. 1997. Emplacement conditions of komatiite magmas from the 3.49 Ga Komati Formation, Barberton Greenstone Belt, South Africa. Earth and Planetary Science Letters, 150: 303-323.

Roeder, P.L., Reynolds, I. 1991. Crystallization of chromite and chromium solubility in basaltic melts. Journal of Petrology, 32(5): 909-934.

Shimizu, K., Komiya, T., Hirose, K., Shimizu, N., Maruyama, S. 2001. Cr-spinel, an excellent micro-container for retaining primitive melts – implications for a hydrous plume origin for komatiites. Earth and Planetary Science Letters, 189: 177-188.

Sisson, T.W., Grove, T.L. 1993. Experimental investigations of the role of H2O in calc-alkaline differentiation and subduction zone magmatism. Contributions to Mineralogy and Petrology, 113: 143-166.

Sobolev, A.V., Asafov, E.V., Gurenko, A.A., Arndt, N.T., Batanova, V.G., Portnyagin, M.V., Garbe-Schönberg, D., Krasheninnikov, S.P. 2016. Komatiites reveal a hydrous Archean deep-mantle reservoir. Nature, 531: 628-632.

Stone, W.E., Deloule, E., Stone, M.S. 2003. Hydromagmatic amphibole in komatiitic, tholeiitic and ferropicritic units, Abitibi greenstone belt, Ontario and Quebec: evidence for Archean wet basic and ultrabasic melts. Mineralogy and Petrology, 77: 39-65.

Stowe, C.W. 1994. Compositions and tectonic settings of chromite deposits through time. Economic Geology, 89: 528-546.

Thy, P. 1995. Low-pressure experimental constraints on the evolution of komatiites. Journal of Petrology, 36(6): 1529-1548.

Ulmer, P. Luth, R.W. 1990. The graphite-COH fluid equilibrium in P, T, fO_2 space: an experimental determination to 30 kbar and 1600°C. Contributions to Mineralogy and Petrology, 106: 265-272.

Viljoen, M.J., Viljoen, R.P. The geology and geochemistry of the lower ultramafic unit of the Onverwacht Group and a proposed new class of igneous rocks. Geological Society of South Africa Special Publication

Watson, E.B., Wark, D.A., Price, J.D., Van Orman, J.A. 2002. Mapping the thermal structure of solid-media pressure assemblies. Contributions to Mineralogy and Petrology, 142: 640-652.

Yudovskaya, M.A., Naldrett, A.J., Woolfe, J.A.S., Costin, G., Kinnaird, J.A. 2015. Reverse compositional zoning in the Uitkomst chromitites as an indication of crystallization in a magmatic conduit. Journal of Petrology, 56(12): 2373-2394.